Supporting Information for "Inferring tectonic plate rotations from InSAR time series"

Yuan-Kai Liu[1], Zhang Yunjun[1,2,3], Mark Simons[1]

[1]Seismological Laboratory, Division of Geological and Planetary Sciences, California Institute of Technology

[2]Now at National Key Laboratory of Microwave Imaging, Aerospace Information Research Institute, Chinese Academy of Sciences

[3]Now at School of Electronic, Electrical and Communication Engineering, University of Chinese Academy of Sciences

Contents of this file

Supplementary Text

Text S1. GNSS network used in this paper

In the Main Text, we utilize the GNSS dataset from Viltres et al. (2022). This work compiles the most recent and complete GNSS-derived velocities from 168 stations across the Arabian plate for the regional kinematic block model. The GNSS velocities closely fit the Arabian plate motion, with the exception of five stations located near and within the Danakil block (Afar depression in the SW of the map). A single Euler pole at 50.93±0.15N, 353.91±0.25E, with a rotation rate of 0.524±0.001/Ma, effectively explains nearly all the GNSS station velocities relative to the ITRF14 reference frame (Figure S13), confirming the large-scale rigidity of the plate (Le Pichon & Kreemer, 2010; Viltres et al., 2022).

In our joint inversion presented in the Main Text (Figure 4), the aim is to demonstrate InSAR's contribution to enhancing GNSS ability to infer the Euler vector when they are limited specifically in the northwest Arabia. Therefore, we only include the 15 GNSS sites located within the InSAR footprint in the NW Arabia (including station HALY, which was used to determine the ITRF2014 Arabian Plate Motion Model).

For the GNSS synthetic tests in Main Text Section 3.3, we further include stations from the eastern side of the Arabian Peninsula to cover a broader range of the rotational field, thereby reducing the uncertainty in the inferred Euler vector. These stations include SQUO in Muscat (Oman), and the four stations used to determine the ITRF2014 Arabian Plate Motion Model (Altamimi et al., 2017): NAMA, JIZN, SOLA, and BAHR. For a rigid plate like Arabia, a sparse but widely distributed GNSS network can adequately constrain the angular velocity vector by properly sampling the rotation field. Consequently, InSAR may not be essential with high-fidelity GNSS stations spanning the plate's width.

Text S2. InSAR velocity

Text S2-1. Velocity and uncertainty estimation

After applying corrections for solid-earth tides (SET), ERA5 weather model, ocean-tidal loading effects (OTL), ionospheric phases, and DEM error estimates, we model the time series at each pixel using the following equation:

$$d(t_k) = a_0 + \dot{a}t_k + a_{c_1}\cos(2\pi t_k) + a_{s_1}\sin(2\pi t_k) + a_{c_2}\cos(4\pi t_k) + a_{s_2}\sin(4\pi t_k) + \epsilon(t_k) \tag{1}$$

We solve for the parameters (intercept a_0, linear rate $\dot{a}$, and annual/semi-annual periodic terms a_{c_1}, a_{c_2}, a_{s_1}, a_{s_2}) using a least-squares approach. The linear rate $\dot{a}$ is extracted as the velocity estimate (Figure S2). We compute the standard deviation of the residuals, $\sigma_{\epsilon(t_k)}$, and propagate it to estimate the velocity uncertainty (Figure S2 and S10), assuming uncorrelated Gaussian errors at all epochs (Fattahi & Amelung, 2015), with:

$$\dot{\sigma}_{\mathrm{v}} = \frac{\sigma_{\epsilon(t_k)}}{\sqrt{\mathrm{N}-6}\sigma_t} \tag{2}$$

where N is the number of epochs (K), N − 6 represents the degrees of freedom in Equation (5), and σ_t is the standard deviation of all time epochs in years.

Velocity maps derived from Sentinel-1 TOPS (Terrain Observation with Progressive Scans) interferograms (Figure S10) exhibit noise, particularly at burst boundaries, manifesting as intra-burst phase ramps and inter-burst discontinuities. These are primarily attributed to ionospheric effects causing azimuthal misregistration, which our split-band ionospheric correction did not fully account for (Gomba et al., 2017; Liang et al., 2019). Our processing only corrects for the range phase group delay caused by spatially smooth Total Electron Content (TEC). While intra-burst phase ramps could be removed by estimating azimuthal misregistration and related ramps due to TEC spatial gradients (Liang et al., 2019), this method relies on detailed quality checks of the estimated TEC gradient, which we consider more susceptible to unwrapping errors in sub-band ionospheric phases. Given our focus on the long-wavelength gradient of the velocity field, we did not address these higher-frequency effects.

The uncertainty of the velocity field (quantified by the standard deviation of the velocity fit) varies spatially, with higher uncertainty in the tracks over Oman and Yemen (the row of Std. in Figure S10). These four tracks also show lower average coherence across all interferograms. Several factors likely contribute to this reduced coherence in Yemen and Oman (typically $\gamma \sim 0.7 - 0.8$) compared to NW Arabia ($\gamma > 0.9$): (1) Steeper terrains, such as the southern Sarawat Mountains (e.g., near Jabal An-Nabī Shu'ayb), with significant elevation changes (< 1 km to 4 km within 100 km), cause geometric decorrelation and phase noise. (2) Tropospheric conditions: Yemen and Oman, located in more tropical latitudes, experience greater water vapor variability (e.g., wet delays of 5–20 cm), contrasting with the more stable, arid climate of NW Arabia. (3) Surface decorrelation: Extensive sand dune fields in Yemen and Oman (e.g., Rub' al Khali) lead to temporal decorrelation due to surface changes, unlike the stable rocky surfaces in NW Arabia.

Text S2-2. Performance of time-series corrections in reducing ramps

To quantify the effectiveness of time-series corrections (solid-earth tides (SET), ERA5 weather model, ocean-tidal loading effects (OTL), ionospheric phases, and DEM error estimates), we assess the agreement between the model-predicted ramp and the ramp observed in the data. We fit linear spatial ramps to the displacement data at each time-series epoch:

$$d(t_k) = r_x x + r_y y + d_r(t_k) = r(t_k) + d_r(t_k) \tag{3}$$

where $d(t_k)$ represents the displacement map at time t_k (the k-th epoch in the time series of K total dates, $t = t_1, t_2, ..., t_k, ..., t_K$). At each t_k, the spatial linear ramp $r(t_k) = r_x x + r_y y$ is defined relative to a reference point and characterized by slopes r_x and r_y (in mm/km) along the longitude (x) and latitude (y) grids, respectively. The term $d_r(t_k)$ represents the residual higher-frequency component of the time-series map. This same linear ramp fitting procedure is applied to the correction models (ERA5, SET, Ionosphere, and OTL). For each epoch, we compute the ramp magnitude $|r_k| = \sqrt{r_x^2 + r_y^2}$. The comparison between the data-derived ramps and the model-predicted ramps is illustrated in Figure S1, highlighting that the ionosphere and troposphere are the primary contributors to these ramps.

We also estimate the ramps of the velocity field using the form:

$$v = r_x x + r_y y + v_r = r + v_r \tag{4}$$

where v is the velocity track. x and y are the east-west and north-south location grid coordinates in kilometers. The parameters r_x and r_y are different than the ones in the time-series ramps in Equations 3. The ramp magnitude is defined as the L-2 norm of the ramp parameters, $|r| = \sqrt{r_x^2 + r_y^2}$, and has a unit of mm/yr/km. We compute the apparent velocity from the each correction term and report their corresponding velocity ramp magnitude (scale to mm/yr per 100 km for readability) in the upper-left corner of Figure 2 (a-h) in the Main Text.

Text S2-3. Uncertainty in the long-wavelength velocity

When characterizing the observational errors in the InSAR velocity fields, we removed quadratic ramps from the velocity fields before semi-variogram fitting (Main Text Section 2.3 and Supplement Text 4-2), yielding noise correlation lengths of approximately 30–100 km. The deramping ensures the inversion will not penalize the spatial coherence at the longest-wavelength signal across the InSAR scene, and the angular velocity vector can fit the long-wavelength gradient from plate motions. Therefore, by design, our Euler pole inversion assumes unbiased long-wavelength ramps in the observations. However, noise at longer wavelengths (e.g., across the whole 250 km track) was not accounted for. Such long-wavelength ramp noise may originate from different sources than smaller-scale noise, including baseline errors or inaccuracies in estimated ionospheric phases.

The low coherence observed in Yemen and Oman suggests the potential for unidentified sub-band ionospheric unwrapping errors in the corresponding InSAR velocity fields. These errors can propagate into the estimated ionospheric phase, introducing uncertainties in the long-wavelength velocity fields, which could bias the inferred Euler pole. To empirically quantify this gradient uncertainty, we adopt the method from Lemrabet, Doin, Lasserre, and Durand (2023) and compute the ramp rate error from the time series.

For each InSAR time-series track, following corrections for solid-earth tides, the ERA5 weather model, and ionospheric effects, we fit linear spatial ramps to each epoch as described in Equation 3. We then parameterized the ramp time series $r(t_k)$ with a temporal function (intercept b_0, linear rate $\dot{b}$, annual and semi-annual periodic terms b_{c_1}, b_{s_1}, b_{c_2}, and b_{s_2}) as shown in Equation (5):

$$r(t_k) = b_0 + \dot{b}t_k + b_{c_1}\cos(2\pi t_k) + b_{s_1}\sin(2\pi t_k) + b_{c_2}\cos(4\pi t_k) + b_{s_2}\sin(4\pi t_k) + \epsilon_r(t_k) \quad (5)$$

Note that the linear rate $\dot{b}$ is primarily governed by the plate motion in ITRF2014. As the Euler pole inversion mainly utilizes long-wavelength velocity gradients, our aim here is to estimate the uncertainty of its empirical proxy: the ramp rate $\dot{b}$. To do this, we compute the ramp in the residuals $\epsilon_r(t_k)$ and determine the standard deviations across all t_k. The standard deviations of the residual ramp parameters in the east-west and north-south directions, $\sigma_{\epsilon_{rx}}$ and $\sigma_{\epsilon_{ry}}$, are linearly propagated to approximate the standard deviation of the velocity ramp rate $\dot{\sigma}_{\text{ramp}}$ (Fattahi & Amelung, 2015; Lemrabet et al., 2023):

$$\dot{\sigma}_{\text{ramp}} = \frac{\sigma_{\text{ramp}}}{\sqrt{\text{N}-6}\sigma_t} \quad (6)$$

where σ_{ramp} represents either $\sigma_{\epsilon_{rx}}$ or $\sigma_{\epsilon_{ry}}$, and $\dot{\sigma}_{\text{ramp}}$ is the corresponding ramp rate uncertainty. N is the number of epochs (K), and $\text{N}-6$ represents the degrees of freedom in Equation (5). σ_t is the standard deviation of all time epochs in years.

For velocity tracks in NW Arabia (Figure), the standard deviations of the east-west ramp rate are approximately 0.0005 mm/year/km, corresponding to about 0.125 mm/year across a 250 km longitude span. The north-south ramp rate error is around 0.0012 mm/year/km, equating to 1.2 mm/year along a 1000 km latitudinal track. Ramp rate errors in Oman and Yemen are significantly higher due to lower coherence and rougher terrain hindering reliable ionospheric phase estimation. The east-west errors range from 0.0016 to 0.004 mm/year/km (0.4 to 1.0 mm/year across 250 km), and the north-south errors range from 0.0023 to 0.0034 mm/year/km (2.3 to 3.4 mm/year along 1000 km). Generally, likely due to stronger north-south ionospheric phase gradients in the region, the north-south ramp rates exhibit larger errors than the east-west ones when residual ionospheric effects are present. Although we estimate this ramp rate error for all the tracks, we did not include this error into the inversion of the Euler pole. While this could be done to re-weight different track's data, the results might not be altered significantly due to the magnitude of the error ($< 10\%$ of the actual plate motion gradient).

Text S3. Euler rotation pole

In this section, we describe the equations of Euler pole inversion using InSAR line-of-sight (LOS) velocity fields.

Text S3-1. The mathematical notation

The Sentinel-1 orbit is defined relative to the International Terrestrial Reference Frame 2014 (ITRF2014). ITRF2014 is an Earth-centered, Earth-fixed (ECEF) reference frame with no net rotation (NNR) of the Earth's surface. Observations of absolute ground motion relative to the satellite are therefore also described in ITRF2014 (Peter, 2021; Stephenson et al., 2022; Lazecký et al., 2023).

If the ground motions can be simplified as rigid rotation of a plate, the line-of-sight (LOS) velocities measured in Sentinel-1, $\mathbf{d}$, can be described as rotation around an Euler vector (McKenzie & Parker, 1967; Morgan, 1968; Cox & Hart, 1986) as

$$\mathbf{d} = \mathbf{G}\ \mathbf{m} \tag{7}$$

$$[P \times 1] = [P \times 3][3 \times 1].$$

The Euler vector, $\mathbf{m}$, denotes the angular velocities in three orthogonal components in the Cartesian coordinates, $\mathbf{m} = [\mathrm{m_x}, \mathrm{m_y}, \mathrm{m_z}]^\intercal$ $(rad/year)$. The Euler pole rotation vector is linearly mapped to the LOS velocities at each pixel by the linear operator $\mathbf{G}$, which is fully determined by the coordinates and the radar line-of-sight vector of each ground pixel i out of a total number of P pixels for which we estimate a deformation velocity

$$\mathbf{G} = \begin{bmatrix} \mathbf{G}^1 \\ \vdots \\ \mathbf{G}^i \\ \vdots \\ \mathbf{G}^P \end{bmatrix} \tag{8}$$

$$i \in [1, \ldots, P],$$

and each row encapsulates three transformation matrices for each pixel independently:

$$\mathbf{G}^i = \mathbf{T}^i_\Lambda\ \mathbf{T}^i_\Theta\ \mathbf{T}^i_\mathrm{X} \tag{9}$$

$$[1 \times 3] = [1 \times 3] \cdot [3 \times 3] \cdot [3 \times 3],$$

where $\mathbf{T}_{\mathrm{X}}^{i}$ is a cross-product matrix to map the rotation Euler pole to the Cartesian velocities at a Cartesian location $\mathbf{r}^i = [x, y, z]$, i.e., $\mathbf{v}(\mathbf{r}^i) = \mathbf{r}^i \times \mathbf{m} = \mathbf{T}_{\mathrm{X}}^{i} \cdot \mathbf{m}$, and

$$\mathbf{T}_{\mathrm{X}}^{i} = \begin{bmatrix} 0 & z & -y \\ -z & 0 & x \\ y & -x & 0 \end{bmatrix}_i . \tag{10}$$

The 3-dimensional location in the Cartesian coordinate $\mathbf{r}^i = [\mathrm{x}, \mathrm{y}, \mathrm{z}]$ is determined by the latitude λ, longitude ϕ, and height h, at pixel i on an assumed ellipsoid with an equatorial radius R_{e} and an eccentricity e (Bowring, 1976; Sanz Subirana et al., 2011a):

$$\mathbf{r}^i = \begin{bmatrix} x \\ y \\ z \end{bmatrix} = R_{\mathrm{e}}(1 - e^2 \sin^2 \lambda)^{-1/2} \begin{bmatrix} 1+h \\ 1+h \\ (1-e^2)+h \end{bmatrix} \cdot \begin{bmatrix} \cos\lambda\cos\phi \\ \cos\lambda\sin\phi \\ \sin\lambda \end{bmatrix} . \tag{11}$$

The matrix $\mathbf{T}_{\Theta}^{i}$ transforms from the Cartesian velocity at a given longitude ϕ and latitude λ into the local planar motion in east, north, and up components (Sanz Subirana et al., 2011b):

$$\mathbf{T}_{\Theta}^{i} = \begin{bmatrix} -\sin\lambda & \cos\lambda & 0 \\ -\sin\phi\cos\lambda & -\sin\phi\sin\lambda & \cos\phi \\ \cos\phi\cos\lambda & \cos\phi\sin\lambda & \sin\phi \end{bmatrix}_i . \tag{12}$$

The velocities in east, north, and up are then projected into the LOS direction of the satellite by the array $\mathbf{T}_{\Lambda}^{i} = [\mathrm{l}_1, \mathrm{l}_2, \mathrm{l}_3]$, yielding the LOS velocity $\mathbf{d}$. $\mathbf{T}_{\Lambda}^{i}$ is a unit vector pointing along the observed motion. It is often called the line-of-sight (LOS) vector in the context of InSAR, along which the range change, or the LOS motion is derived from the phase interferometry. Note that any motion in the Euclidean space can be represented as a LOS motion with a magnitude along its unit vector of motion. Thus, this projection unit vector can be generalized to map between the east, north, up components and any 3 dimensional motion, including observations from InSAR range change, radar or optical image offset tracking, and two- or three-component GNSS displacements. In such case, $\mathbf{d}$ can be populated by east, north, and up velocities of multiple stations along the single-column vector. Accordingly, $\mathbf{T}_\Lambda^i = [1, 0, 0]$ corresponds to the east row of $\mathbf{d}$, $\mathbf{T}_\Lambda^i = [0, 1, 0]$ corresponds to the north row, and $\mathbf{T}_\Lambda^i = [0, 0, 1]$ corresponds to the up row, respectively. But, one would remove the vertical component from GNSS in a rotation problem on Earth's surface because it will never be fitted. In our special case of single-component InSAR velocity where the LOS projection at each pixel is dictated by the satellite incidence angle θ and azimuth angle ψ, we can write the projection vector as

$$\mathbf{T}_\Lambda^i = \begin{bmatrix} -\sin\theta\sin\psi \\ \sin\theta\cos\psi \\ \cos\theta \end{bmatrix}_i^\intercal . \tag{13}$$

Note that the plate motion can be measured because incidence and azimuth angles vary across the SAR scene, so θ and ψ here should differ from pixel to pixel. Plug in Equation 8 to 13, each row of $\mathbf{G}^i$ can be constructed as

$$\mathbf{G}^i = \begin{bmatrix} -\sin\theta\sin\psi \\ \sin\theta\cos\psi \\ \cos\theta \end{bmatrix}_i^\intercal \begin{bmatrix} -\sin\lambda & \cos\lambda & 0 \\ -\sin\phi\cos\lambda & -\sin\phi\sin\lambda & \cos\phi \\ \cos\phi\cos\lambda & \cos\phi\sin\lambda & \sin\phi \end{bmatrix}_i \begin{bmatrix} 0 & z & -y \\ -z & 0 & x \\ y & -x & 0 \end{bmatrix}_i , \tag{14}$$

and Equation 7 can be solved simultaneously for all P InSAR pixels, from one or more orbital tracks. The above expression generates an absolute velocity in the reference frame. However, InSAR measurements are always described with respect to a reference point at $\mathbf{r}^*$. There is an unknown constant shift, b, between the measured relative velocity and the absolute velocity in ITRF, $\mathbf{d}^*$ by $\mathbf{d} = \mathbf{d}^* + b$. This shift is track-specific and represents the absolute plate motion at the reference pixel when the atmospheric noise and the unrecognized internal deformation at that pixel can be ignored. Unless pre-determined by independent GNSS, we need to estimate these shifts and the Euler pole simultaneously by

$$\mathbf{d}^* = \mathbf{G}^+ \, \mathbf{m}^+ \quad , \tag{15}$$

where the model parameter vector having the shift term in this InSAR track becomes

$$\mathbf{m}^+ = \begin{bmatrix} \mathrm{m_x} \\ \mathrm{m_y} \\ \mathrm{m_z} \\ b \end{bmatrix} \quad . \tag{16}$$

And, we append a column of ones, $\mathbb{1}$, to the linear operator

$$\mathbf{G}^+ = \begin{bmatrix} \mathbf{G} & \mathbb{1} \end{bmatrix} \quad . \tag{17}$$

However, since the similarity of the azimuth angles across the scene (varies $< 1.6°$), InSAR LOS velocity with residual noise permits high trade-offs between the pole parameters. The extra unknown shifts in the problem only exacerbate these trade-offs. Consequently, a biased Euler pole can be deceptively compensated by a floating shift for the whole track, fitting the observation equally well. Alternatively, we can adjust the linear model to a common reference pixel in data by subtracting the row corresponding to the reference pixel, $\mathbf{G}^* = \mathbf{G} - \mathbf{G}_{\mathbf{r}^*}$. This approach offers two advantages: it avoids additional trade-offs in model parameters and references the linear model to the same reference point as in the InSAR measurements and their observational errors. The formulation we use becomes

$$\mathbf{d}^* = \mathbf{G}^* \, \mathbf{m} \quad . \tag{18}$$

Text S3-2. Transformation between the Cartesian and Spherical expressions

The Euler pole $(\hat{\mathrm{m}}_{\mathrm{x}}, \hat{\mathrm{m}}_{\mathrm{y}}, \hat{\mathrm{m}}_{\mathrm{z}})$ in ECEF Cartesian coordinates can be transformed to the spherical expression (pole latitude λ_{p}, pole longitude ϕ_{p}, and pole angular velocity ω_{p})

$$\begin{cases} \lambda_{\mathrm{p}} = \arctan\left(\dfrac{\mathrm{m_z}}{\sqrt{\mathrm{m_x^2} + \mathrm{m_y^2}}}\right) \\ \phi_{\mathrm{p}} = \arctan\left(\dfrac{\mathrm{m_y}}{\mathrm{m_x}}\right) \\ \omega_{\mathrm{p}} = |\mathbf{m}| = \sqrt{\mathrm{m_x^2} + \mathrm{m_y^2} + \mathrm{m_z^2}} \end{cases} \tag{19}$$

and vice versa

$$\mathbf{m} = w_{\mathrm{p}} \begin{bmatrix} \cos\lambda_{\mathrm{p}} \cos\phi_{\mathrm{p}} \\ \cos\lambda_{\mathrm{p}} \sin\phi_{\mathrm{p}} \\ \sin\lambda_{\mathrm{p}} \end{bmatrix} \quad . \tag{20}$$

The transformation of the model covariance matrix from the Cartesian to Spherical expression is through a Jacobian matrix, $\mathbf{J}_{\mathrm{C2S}}$ (Goudarzi et al., 2014):

$$\hat{\mathbf{C}}_{\mathrm{m}}^{\mathrm{sph}} = \mathbf{J}_{\mathrm{C2S}} \hat{\mathbf{C}}_{\mathrm{m}} \mathbf{J}_{\mathrm{C2S}}^{\intercal} \quad , \tag{21}$$

where

$$\mathbf{J}_{\mathrm{C2S}} = \begin{bmatrix} \dfrac{\partial\lambda_{\mathrm{p}}}{\partial\mathrm{m_x}} & \dfrac{\partial\lambda_{\mathrm{p}}}{\partial\mathrm{m_y}} & \dfrac{\partial\lambda_{\mathrm{p}}}{\partial\mathrm{m_z}} \\ \dfrac{\partial\phi_{\mathrm{p}}}{\partial\mathrm{m_x}} & \dfrac{\partial\phi_{\mathrm{p}}}{\partial\mathrm{m_y}} & \dfrac{\partial\phi_{\mathrm{p}}}{\partial\mathrm{m_z}} \\ \dfrac{\partial\omega_{\mathrm{p}}}{\partial\mathrm{m_x}} & \dfrac{\partial\omega_{\mathrm{p}}}{\partial\mathrm{m_y}} & \dfrac{\partial\omega_{\mathrm{p}}}{\partial\mathrm{m_z}} \end{bmatrix} = \begin{bmatrix} \dfrac{-\mathrm{m_x m_z}}{w_{\mathrm{p}}^2\sqrt{\mathrm{m_x^2}+\mathrm{m_y^2}}} & \dfrac{-\mathrm{m_y m_z}}{w_{\mathrm{p}}^2\sqrt{\mathrm{m_x^2}+\mathrm{m_y^2}}} & \dfrac{\sqrt{\mathrm{m_x^2}+\mathrm{m_y^2}}}{w_{\mathrm{p}}^2} \\ \dfrac{-\mathrm{m_y}}{\mathrm{m_x^2}+\mathrm{m_y^2}} & \dfrac{\mathrm{m_x}}{\mathrm{m_x^2}+\mathrm{m_y^2}} & 0 \\ \dfrac{\mathrm{m_x}}{w_{\mathrm{p}}} & \dfrac{\mathrm{m_y}}{w_{\mathrm{p}}} & \dfrac{\mathrm{m_z}}{w_{\mathrm{p}}} \end{bmatrix} \quad . \tag{22}$$

The inverse transformation from the Spherical to Cartesian expression is through:

$$\hat{\mathbf{C}}_{\mathrm{m}} = \mathbf{J}_{\mathrm{S2C}} \hat{\mathbf{C}}_{\mathrm{m}}^{\mathrm{sph}} \mathbf{J}_{\mathrm{S2C}}^{\intercal} \quad , \tag{23}$$

where

$$\mathbf{J}_{\mathrm{S2C}} = \begin{bmatrix} \dfrac{\partial \mathrm{m_x}}{\partial \lambda_\mathrm{p}} & \dfrac{\partial \mathrm{m_x}}{\partial \phi_\mathrm{p}} & \dfrac{\partial \mathrm{m_x}}{\partial w_\mathrm{p}} \\ \dfrac{\partial \mathrm{m_y}}{\partial \lambda_\mathrm{p}} & \dfrac{\partial \mathrm{m_y}}{\partial \phi_\mathrm{p}} & \dfrac{\partial \mathrm{m_y}}{\partial w_\mathrm{p}} \\ \dfrac{\partial \mathrm{m_z}}{\partial \lambda_\mathrm{p}} & \dfrac{\partial \mathrm{m_z}}{\partial \phi_\mathrm{p}} & \dfrac{\partial \mathrm{m_z}}{\partial w_\mathrm{p}} \end{bmatrix} = \begin{bmatrix} -w_\mathrm{p} \sin \lambda_\mathrm{p} \cos \phi_\mathrm{p} & -w_\mathrm{p} \cos \lambda_\mathrm{p} \sin \phi_\mathrm{p} & \cos \lambda_\mathrm{p} \cos \phi_\mathrm{p} \\ -w_\mathrm{p} \sin \lambda_\mathrm{p} \sin \phi_\mathrm{p} & w_\mathrm{p} \cos \lambda_\mathrm{p} \cos \phi_\mathrm{p} & \cos \lambda_\mathrm{p} \sin \phi_\mathrm{p} \\ w_\mathrm{p} \cos \lambda_\mathrm{p} & 0 & \sin \lambda_\mathrm{p} \end{bmatrix} . \tag{24}$$

Text S4. Formulation of the linear problem

Text S4-1. An example of linear operator, G

Each pixel in InSAR data contributes the pixel-wise LOS velocity, d_i, to one row of the $\mathbf{d}^*$ vector in Equation (12). Each pixel in InSAR data has the unique coordinates and radar imaging geometry that dictate each row, $\mathbf{G}_i = [g_{i1}, g_{i2}, g_{i3}]$ in the linear operator $\mathbf{G}$ (using Equation (8)), such that $d_i = \mathbf{G}_i\mathbf{m}$. We keep the 1-by-3 vector $[g_{i1}, g_{i2}, g_{i3}]$ in a variable form for the convenience of notation, where the first subscript index i is the pixel index and the second subscript index is the column index in $\mathbf{G}$. With total P pixels of velocity observations, we have $\mathbf{d}$ (size of P-by-1) and a design matrix $\mathbf{G}$ (size of P-by-3):

$$\mathbf{G} = \begin{bmatrix} g_{11} & g_{12} & g_{13} \\ & \vdots & \\ g_{i1} & g_{i2} & g_{i3} \\ & \vdots & \\ g_{P1} & g_{P2} & g_{P3} \end{bmatrix} \quad . \tag{25}$$

After constructing the operator $\mathbf{G}$, we subtract the row corresponds to the reference pixel, $\mathbf{G}^* = \mathbf{G} - \mathbf{G}_{\mathbf{r}^*}$, and follow the formulation in Equation 18 to solve the problem with any least-squares method. The example of the linear operator $\mathbf{G}$ is shown in Figure S7.

The P pixels of velocity observations ($\mathbf{d}$) can be acquired from one or several satellite tracks as long as the pixel-wise LOS velocity d_i corresponds to the unique radar imaging geometry used in the linear operator $\mathbf{G}_i$. For example, having totally Q tracks of InSAR velocity fields (e.g., multiple ascending and descending), we concatenate the linear operator in the vertical direction as

$$\mathbf{G} = \begin{bmatrix} \mathbf{g}_1^1 & \mathbf{g}_2^1 & \mathbf{g}_3^1 \\ \mathbf{g}_1^2 & \mathbf{g}_2^2 & \mathbf{g}_3^2 \\ \vdots & \vdots & \vdots \\ \mathbf{g}_1^q & \mathbf{g}_2^q & \mathbf{g}_3^q \\ \vdots & \vdots & \vdots \\ \mathbf{g}_1^Q & \mathbf{g}_2^Q & \mathbf{g}_3^Q \end{bmatrix} \quad , \tag{26}$$

where in each row, $\mathbf{g}_1^q$, $\mathbf{g}_2^q$, $\mathbf{g}_3^q$ denotes the column vectors in Equation 25 for the q-th InSAR track:

$$\mathbf{g_1^q} = \begin{bmatrix} g_{11} \\ \vdots \\ g_{i1} \\ \vdots \\ g_{P_q 1} \end{bmatrix}, \mathbf{g_2^q} = \begin{bmatrix} g_{12} \\ \vdots \\ g_{i2} \\ \vdots \\ g_{P_q 2} \end{bmatrix}, \mathbf{g_3^q} = \begin{bmatrix} g_{13} \\ \vdots \\ g_{i3} \\ \vdots \\ g_{P_q 3} \end{bmatrix} \quad . \tag{27}$$

The pixel index i ranges from 1 to the total number of pixels, P_q, in the q-th InSAR track.

Text S4-2. Observational covariance matrix, $\mathbf{C_d}$

We characterize the observational error in InSAR-derived velocities using the data covariance matrix, which captures the variance and covariance features Hanssen (2001). The data covariance matrix has a dimension of P-by-P (P being the number of pixels in an InSAR track) and consists of two components,

$$\mathbf{C}_{\mathrm{d}} = \mathbf{C}_{\mathrm{d_t}} + \mathbf{C}_{\mathrm{d_s}} \quad . \tag{28}$$

The temporal term, $\mathbf{C}_{\mathrm{d_t}}$, is a diagonal matrix populated with the variances of the velocity estimates at pixel i, σ_i, determined by the functional-fit residuals assuming uniform Gaussian errors at all epochs as

$$\mathbf{C}_{\mathrm{d_t}} = \begin{bmatrix} \sigma_1 & 0 & 0 \\ 0 & \ddots & 0 \\ 0 & 0 & \sigma_P \end{bmatrix} \quad . \tag{29}$$

The spatial term, $\mathbf{C}_{\mathrm{d_s}}$, accounts for the stationary and isotropic noise correlation between nearby pixels, which we attribute to the remaining atmospheric effects after corrections. We use sample semi-variograms $\gamma(h)$ to estimate the InSAR variances as a function of distance between any pixel pair. Due to potential bias from the imperfect assumption of the stationary process of noise, we do not use a sample covariogram method. However, it should be equivalent to the sample semi-variogram method in an ideal case.

The discrete sample semi-variogram value for binned distance class h_c is

$$\gamma(h_c) = \frac{1}{2\mathrm{N}} \sum_{\substack{i=1 \\ \|\mathbf{r}_i - \mathbf{r}_j\| \simeq h_c}}^{N} [v(\mathbf{r}_i) - v(\mathbf{r}_j)]^2 \quad , \tag{30}$$

where N being the number of data-point pairs at locations $\mathbf{r}_i$ and $\mathbf{r}_j$ such that $\|\mathbf{r}_i - \mathbf{r}_j\|$ falls inside a distance bin h_c. Thus, when assuming isotropic noise, the semi-variogram depends only on distance h between data points.

We first uniformly downsample the velocity fields to approximately 2.5 km posting. The goal here is to quantify the intermediate range noise structure without sacrificing the ability to fit the longest-wavelength plate motion, thus we first remove a quadratic ramp from the velocity fields before sampling the semi-variograms (Figure S5). The quadratic ramp is parameterized in the form of $v = \mathrm{u}x^2 + \mathrm{v}y^2 + \mathrm{w}xy + \mathrm{a}x + \mathrm{b}y + \mathrm{c}$, where v is the velocity track. x and y are the east-west and north-south location grid coordinates in kilometers. The parameters a, b, c, u, v, and w are estimated in a least-squares sense. Then, we randomly pick velocity pairs $v(\mathbf{r}_i)$ and $v(\mathbf{r}_j)$ with distances h up to 300 km for each track. We then form the sample semi-variogram $\gamma(h)$ by taking the average in 1-km intervals. The data variance is estimated from the level at which the sample semi-variogram $\gamma(h)$ forms a plateau (called "sill") at distances larger than the characteristic length scale of correlation (Figure S6).

For a continuous description of the variogram we fit functions to the sample-variogram. The variance is a positive-definite function. Therefore, we use a function type ensuring positive definiteness, an inverse exponential decay function as

$$\gamma(h) = -(A^2)\exp(\frac{-h}{\lambda}) + \sigma \quad , \tag{31}$$

where A is the scaling factor, λ is the characteristic length of the correlation, and σ is the sill. The covariance function is then the mirror of the semi-variogram, expressing the degeneration of the covariance. In the presence of white noise, the covariance function has a step at a zero lag. We thus parameterize the spatial covariance matrix, $\mathbf{C}_{d_s}$ using the covariance function

$$\mathbf{C}_{d_s} = \mathbf{C}(h) = (A^2)\exp(\frac{-h}{\lambda}) + \sigma \quad . \tag{32}$$

Based on this function, we create the spatial covariance matrix, $\mathbf{C}_{\mathrm{d_s}}$. The diagonals are populated with a constant value of σ, the off-diagonals are computed based on the distance separations of pixel pairs, h. Our covariance matrices are shown in Figure S8 and S9.

Text S5. Unwrapping error correction

Unwrapping errors refer to the wrong integer numbers of cycles (2π radians) being added to the interferometric phase during the two-dimensional phase unwrapping. Unwrapping errors will propagate to the Small-BAseline-Subset (SBAS) time-series phases and bias the phase history. Our datasets contain unwrapping errors near Wadi Arabah valley in Egypt in tracks A058, D094 (the data from these two tracks in the Sinai subplate are not being used in the analysis described in the Main Text), and north-west Arabia track D021.

Since the errors are potentially due to intense tropospheric delay variation occurring in areas with sharp elevation change, we first remove the ERA5 model predicted phase from the wrapped interferograms and unwrap the phase (Jolivet et al., 2011). In addition to the stratified tropospheric phases, we also remove the ionospheric phases estimated from the split-spectrum method from the interferograms to further reduce the spatial phase gradients. These approaches do not clear all the unwrapping errors, leaving considerable remaining discontinuities in the velocity fields. Thus, other more delicate methods to correct for the unwrapping errors are needed (Figure S14).

Several methods to correct for the unwrapping errors, such as bridging (Biggs et al., 2007; Yunjun et al., 2019) and phase closure (Yunjun et al., 2019) rely on the properly labeled phase connected areas, called connected components. Each component is isolated by the unwrapping error to its neighboring one. However, the connected components in SNAPHU algorithm are not always identified and labeled correctly (also seen in Oliver-Cabrera, Jones, Yunjun, and Simard (2022)). Thus, many of the unwrapping errors present in our datasets are not properly labeled (Figure S14). Therefore, we attempt to come up with a way to re-generate the informative labels quantitatively, so that we can apply the unwrapping error correction based on these new labels.

We first make sure to minimize the phase gradients in the interferograms as much as possible before unwrapping. We remove the stratified tropospheric phases using either ERA5 or GACOS. We also remove the estimated ionospheric phases. To re-generate a better set of connected components for all pixels, we compute the number of triplets having non-zero integer ambiguity of closure phase (T_{int} in Yunjun et al. (2019)). Pixels in the same connected region would have the same number of non-zero closure triplets. Thus, we run a clustering algorithm to group the areas based on their T_{int} and generate a new set of connected components. To estimate the number of integer ambiguities in the network, we assume triplet phases should be within $\pm\pi$ and implement a region-based inversion to minimize the regularized L1-norm. To reduce computation, instead of inverting every pixel for the integer ambiguity, we randomly select 100 pixels for each common connected component and conduct the inversion. The median of inverted numbers is used for all pixels within this common component and removed from the phase time series (Yunjun et al., 2019). This approach successfully mitigate the unwrapping errors in tracks D094 over the Sinai Peninsula (Figure S14), D021 in the northwest Arabia, and A058 along the Nile river.

References

Altamimi, Z., Métivier, L., Rebischung, P., Rouby, H., & Collilieux, X. (2017). ITRF2014 plate motion model. *Geophysical Journal International*, *209*, 1906–1912. doi: 10.1093/gji/ggx136

Biggs, J., Wright, T., Lu, Z., & Parsons, B. (2007). Multi-interferogram method for measuring interseismic deformation: Denali Fault, Alaska. *Geophysical Journal International*, *170*, 1165–1179. doi: 10.1111/j.1365-246X.2007.03415.x

Bowring, B. R. (1976). Transformation from spatial to geographical coordinates. *Surv. Rev.*, *23*, 323–327. doi: 10.1179/sre.1976.23.181.323

Cox, A., & Hart, R. B. (1986). *Plate tectonics: How it works.* John Wiley & Sons.

Fattahi, H., & Amelung, F. (2015). InSAR bias and uncertainty due to the systematic and stochastic tropospheric delay. *J. Geophys. Res. Solid Earth*, *120*, 8758–8773. doi: 10.1002/2015JB012419

Gomba, G., Rodríguez González, F., & De Zan, F. (2017). Ionospheric Phase Screen Compensation for the Sentinel-1 TOPS and ALOS-2 ScanSAR Modes. *IEEE Trans. Geosci. Remote Sens.*, *55*, 223–235. doi: 10.1109/TGRS.2016.2604461

Goudarzi, M. A., Cocard, M., & Santerre, R. (2014). EPC: Matlab software to estimate Euler pole parameters. *GPS Solut*, *18*, 153–162. doi: 10.1007/s10291-013-0354-4

Hanssen, R. F. (2001). *Radar Interferometry: Data Interpretation and Error Analysis.* Springer Science & Business Media.

Jolivet, R., Grandin, R., Lasserre, C., Doin, M.-P., & Peltzer, G. (2011). Systematic InSAR tropospheric phase delay corrections from global meteorological reanalysis data. *Geophys. Res. Lett.*, *38*. doi: 10.1029/2011GL048757

Lazecký, M., Hooper, A. J., & Piromthong, P. (2023). InSAR-derived horizontal velocities in a global reference frame. *Geophys. Res. Lett.*, *50*, e2022GL101173. doi: 10.1029/2022GL101173

Lemrabet, L., Doin, M.-P., Lasserre, C., & Durand, P. (2023). Referencing of continental-scale InSAR-derived velocity fields: Case study of the eastern Tibetan plateau. *J. Geophys. Res. Solid Earth*, *128*, e2022JB026251. doi: 10.1029/2022JB026251

Le Pichon, X., & Kreemer, C. (2010). The Miocene-to-present kinematic evolution of the eastern Mediterranean and Middle East and its implications for dynamics. *Annu. Rev. Earth Planet. Sci.*, *38*, 323–351. doi: 10.1146/annurev-earth-040809-152419

Liang, C., Agram, P., Simons, M., & Fielding, E. J. (2019). Ionospheric Correction of InSAR Time Series Analysis of C-band Sentinel-1 TOPS Data. *IEEE Trans. Geosci. Remote Sens.*, *57*, 6755–6773. doi: 10.1109/TGRS.2019.2908494

McKenzie, D. P., & Parker, R. L. (1967). The North Pacific: An example of tectonics on a sphere. *Nature*, *216*, 1276–1280. doi: 10.1038/2161276a0

Morgan, W. J. (1968). Rises, trenches, great faults, and crustal blocks. *J. Geophys. Res. 1896-1977*, *73*, 1959–1982. doi: 10.1029/JB073i006p01959

Oliver-Cabrera, T., Jones, C. E., Yunjun, Z., & Simard, M. (2022). InSAR phase unwrapping error correction for rapid repeat measurements of water level change in wetlands. *IEEE Trans. Geosci. Remote Sensing*, *60*, 1–15. doi: 10.1109/TGRS.2021.3108751

Peter, H. (2021). *Copernicus Sentinel-1, -2 and -3 Precise Orbit Determination Service*

(CPOD) (Handbook). European Space Agency (ESA).

Sanz Subirana, J., Juan Zornoza, J., & Hernández-Pajares, M. (2011a). *Ellipsoidal and cartesian coordinates conversion - Navipedia.* https://gssc.esa.int/navipedia/index.php/Ellipsoidal_and_Cartesian_Coordinates_Conversion.

Sanz Subirana, J., Juan Zornoza, J., & Hernández-Pajares, M. (2011b). *Transformations between ECEF and ENU coordinates - Navipedia.* https://gssc.esa.int/navipedia/index.php/Transformations_between_ECEF_and_ENU_coordinates.

Stephenson, O. L., Liu, Y.-K., Yunjun, Z., Simons, M., Rosen, P., & Xu, X. (2022). The impact of plate motions on long-wavelength InSAR-derived velocity fields. *Geophys. Res. Lett.*, *49*, e2022GL099835. doi: 10.1029/2022GL099835

Viltres, R., Jónsson, S., Alothman, A., Liu, S., Leroy, S., Masson, F., ... Reilinger, R. (2022). Present-day motion of the Arabian plate. *Tectonics*, *41*, e2021TC007013. doi: 10.1029/2021TC007013

Yunjun, Z., Fattahi, H., & Amelung, F. (2019). Small baseline InSAR time series analysis: Unwrapping error correction and noise reduction. *Computers & Geosciences*, *133*, 104331. doi: 10.1016/j.cageo.2019.104331

Zheng, Y., Fattahi, H., Agram, P., Simons, M., & Rosen, P. (2022). On closure phase and systematic bias in multilooked SAR interferometry. *IEEE Trans. Geosci. Remote Sens.*, *60*, 1–11. doi: 10.1109/TGRS.2022.3167648

Table S1. InSAR-derived Euler vector parameters of the Arabian plate

Spherical expression[a]	Unit[c]	Value	1σ
Pole latitude	deg	49.7081	1.7108
Pole longitude	deg	-7.8751	3.7392
Rotation rate	deg/Ma	0.5514	0.0178
	mas/yr	1.9849	0.0639
Cartesian expression[b]	Unit	Value	1σ
m_x	deg/Ma	0.3532	0.0206
	mas/yr	1.2715	0.0742
m_y	deg/Ma	-0.0489	0.0243
	mas/yr	-0.1759	0.0875
m_z	deg/Ma	0.4206	0.0105
	mas/yr	1.5140	0.0380
The full covariance, $\mathbf{C}_m$ (mas^2/yr^2)			
	xx	xy	xz
	2.67062164e-11	-1.08156340e-11	4.67775869e-12
	yy	yz	zz
	3.71520731e-11	9.74410320e-12	6.99011278e-12

[a] The spherical expression is often referred to as the Euler pole location and the rotation rate.

[b] The Cartesian expression denotes the angular velocity vector. The three orthogonal axes x, y, and z aligns with the (0°N, 0°E), (0°N, 90°E), and 90°N components, respectively.

[c] deg: degrees. Ma: million years. yr: years. mas: milliarcsecond. rad: radian.

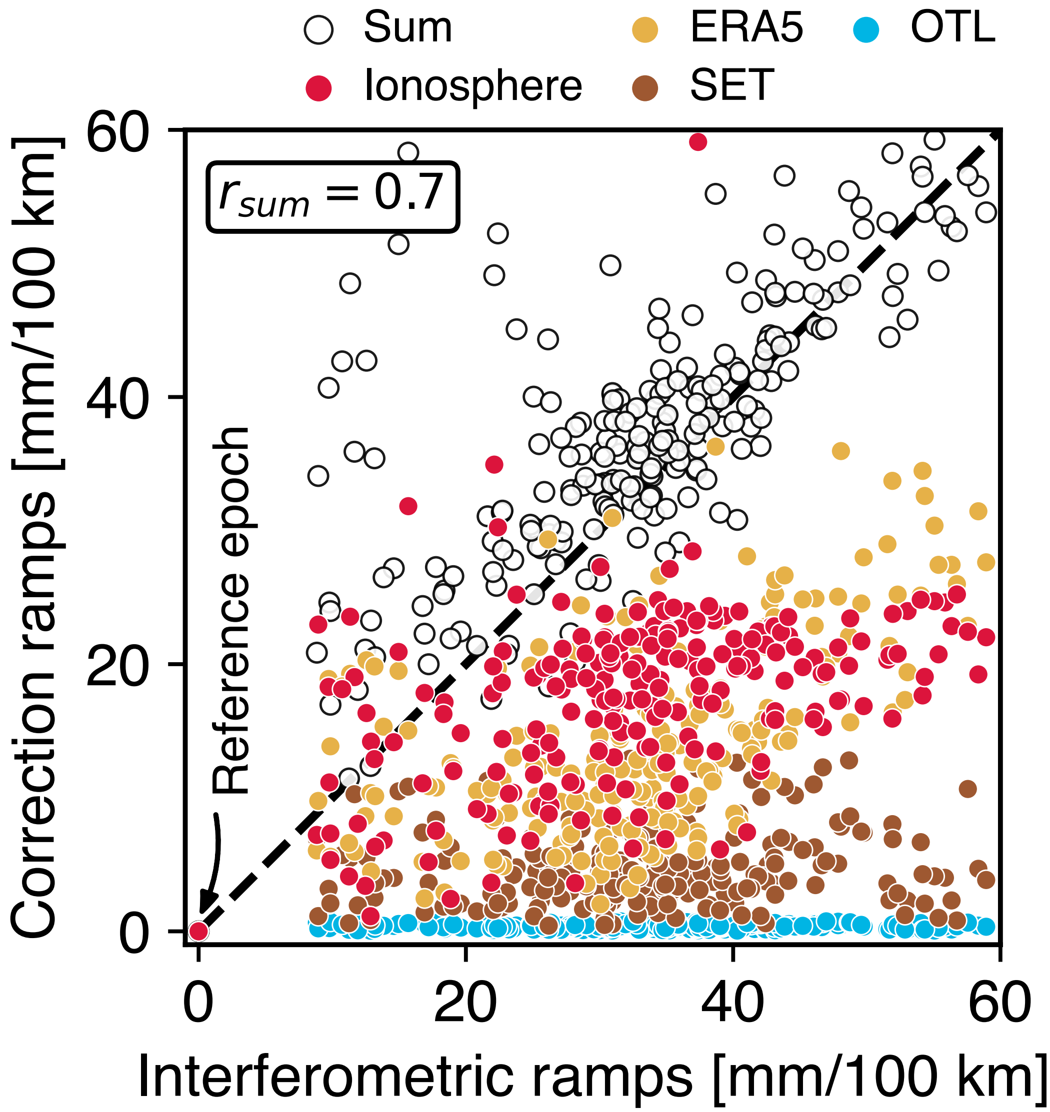

Figure S1. Fitted ramp magnitude at each time-series epoch (observations on x-axis and correction predictions on y-axis). r_{sum} is the correlation coefficient between ramps predicted by the sum of all correction terms and the observed ramps.

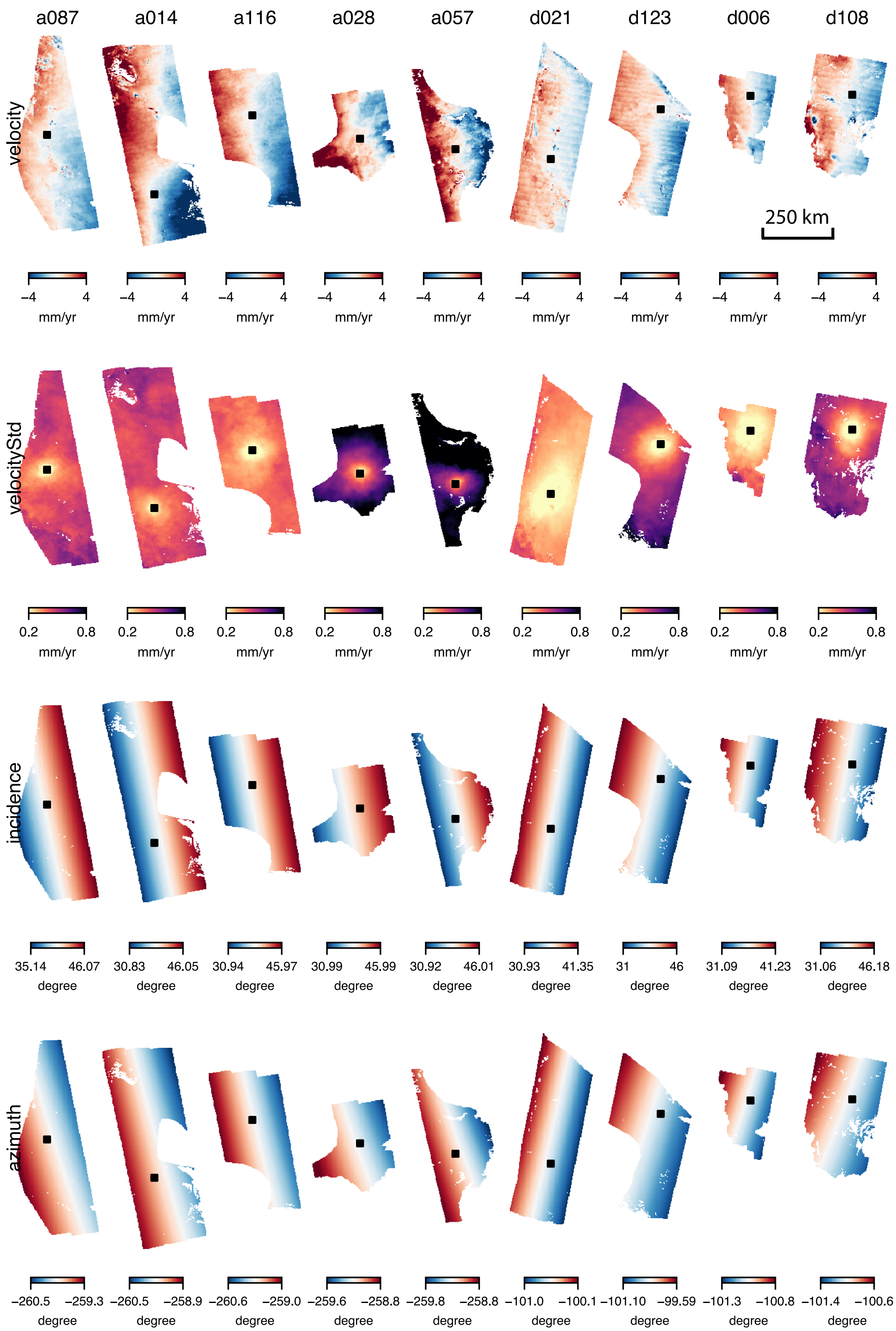

Figure S2. Caption next page.

Figure S2. The LOS velocity fields, standard deviations, incidence, and azimuth angles from all nine Sentinel-1 tracks. Velocities and errors are referenced to our prior-selected reference points, the black squared markers.

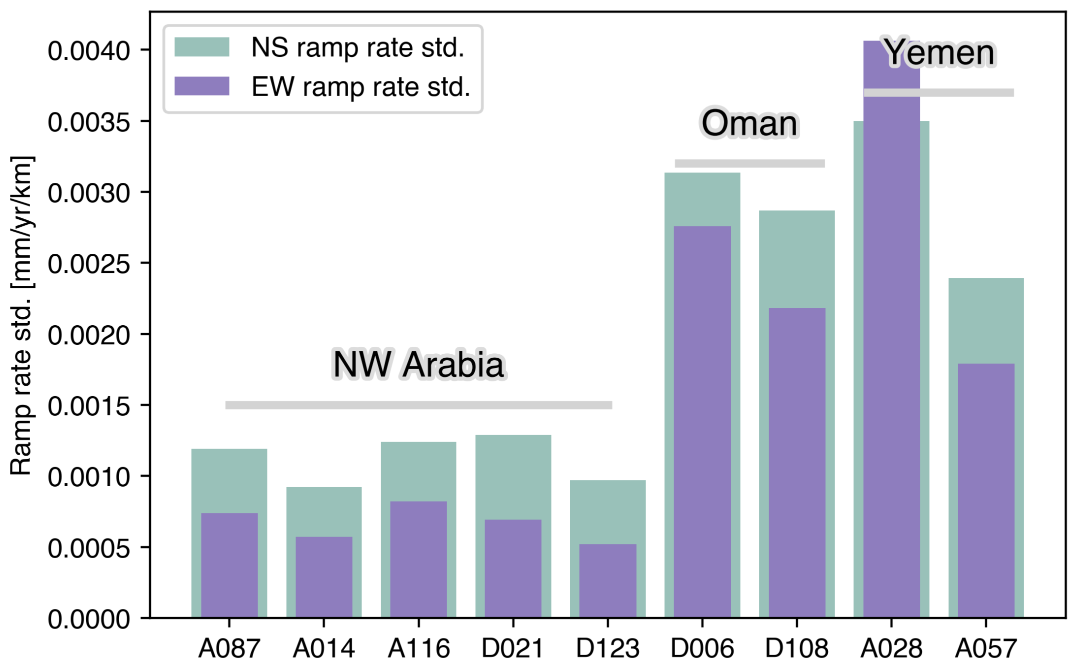

Figure S3. Standard deviations of the ramp rate, corresponding to $\dot{\sigma}_{\text{ramp}}$ in Equation 6.

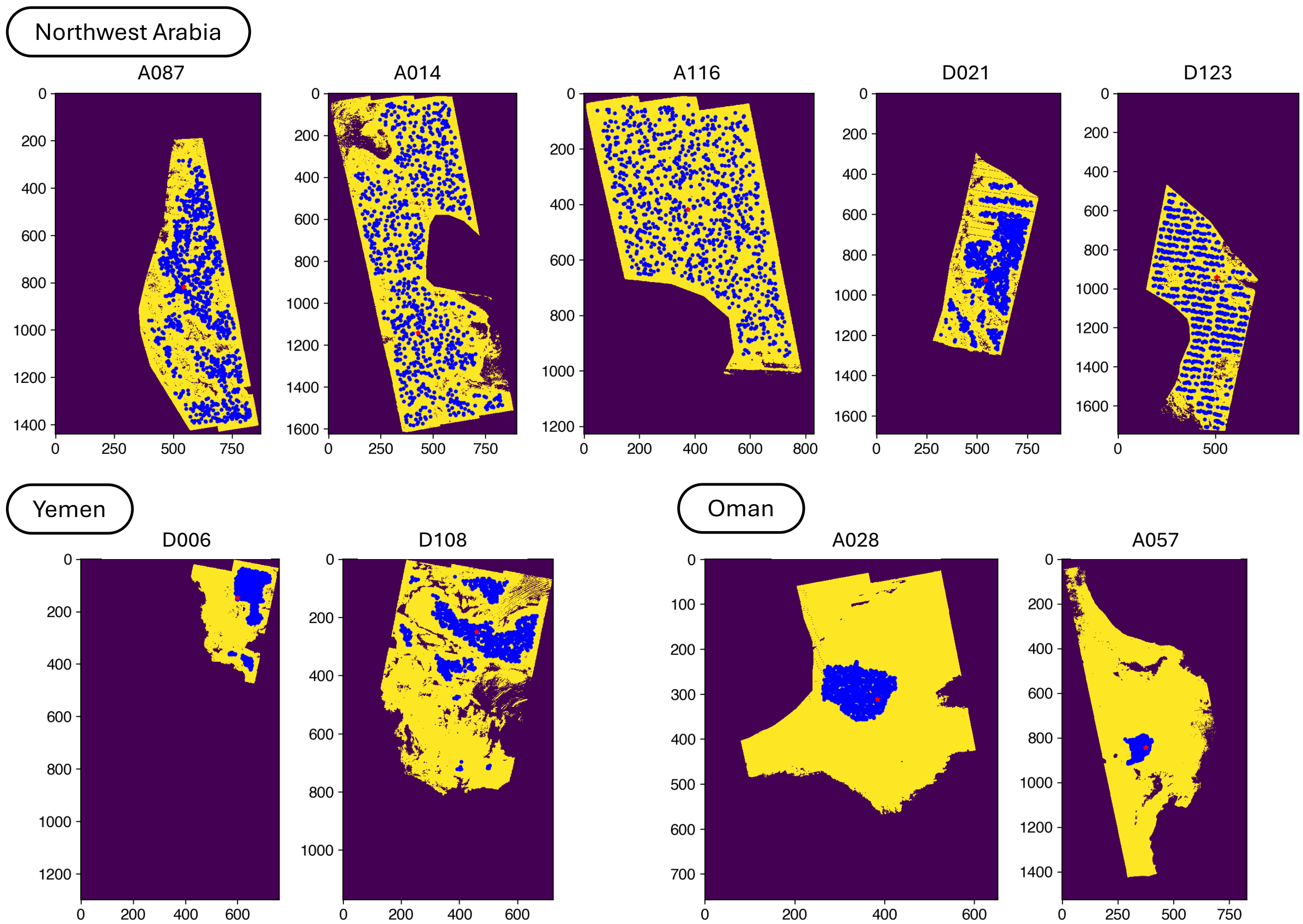

Figure S4. The 1,000 sets of randomly selected reference points. The criteria for random selection is: temporal coherence > 0.9 (Yunjun et al., 2019), cumulative closure phase exceeds three times the standard deviation (Zheng et al., 2022), an elevation below 1500 m, and be at least 25 km from masked areas. See the Main Text Section 2.3.

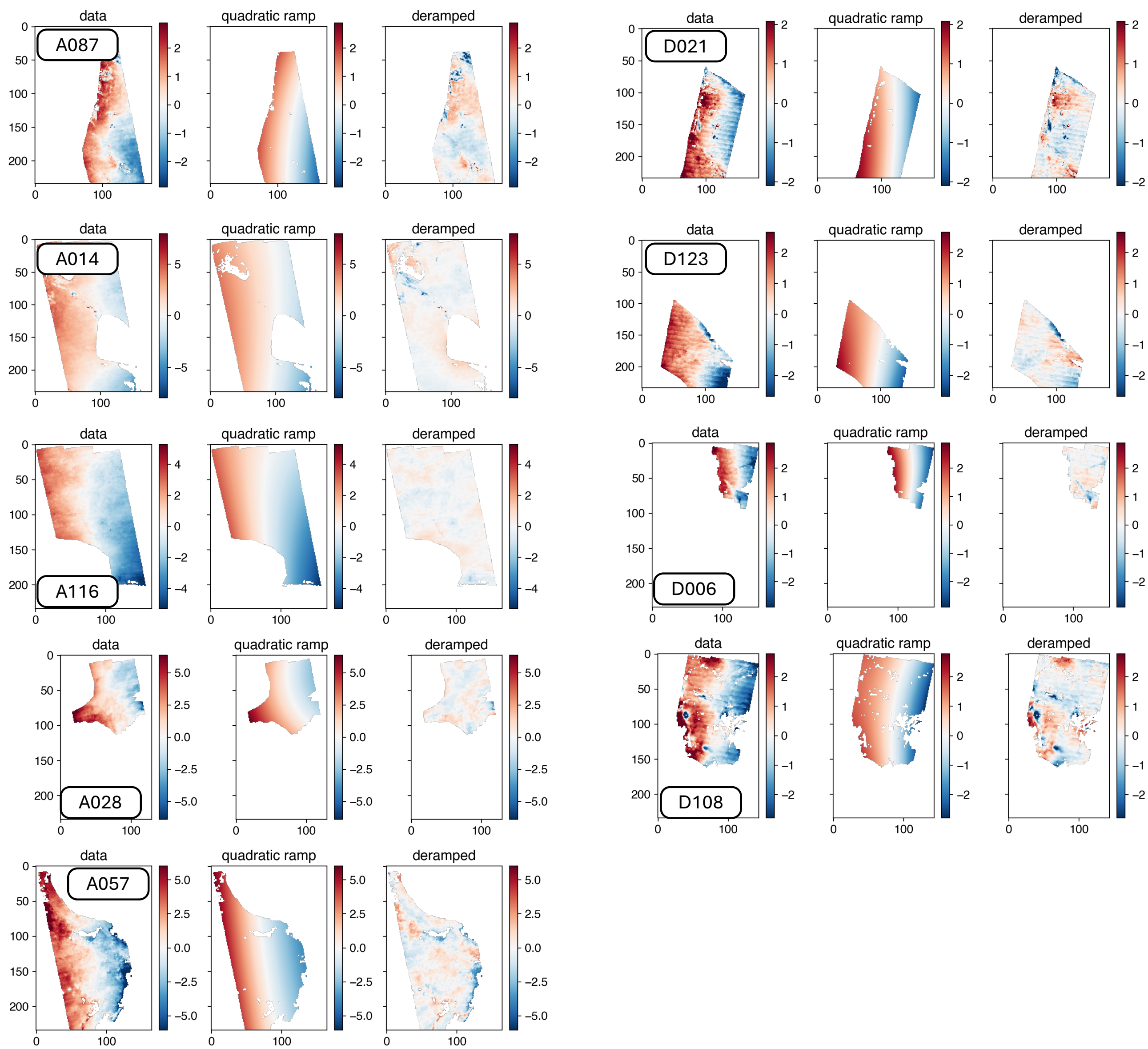

Figure S5. Quadratic deramping before sampling the semi-variograms. See Suppl. Text S4-2.

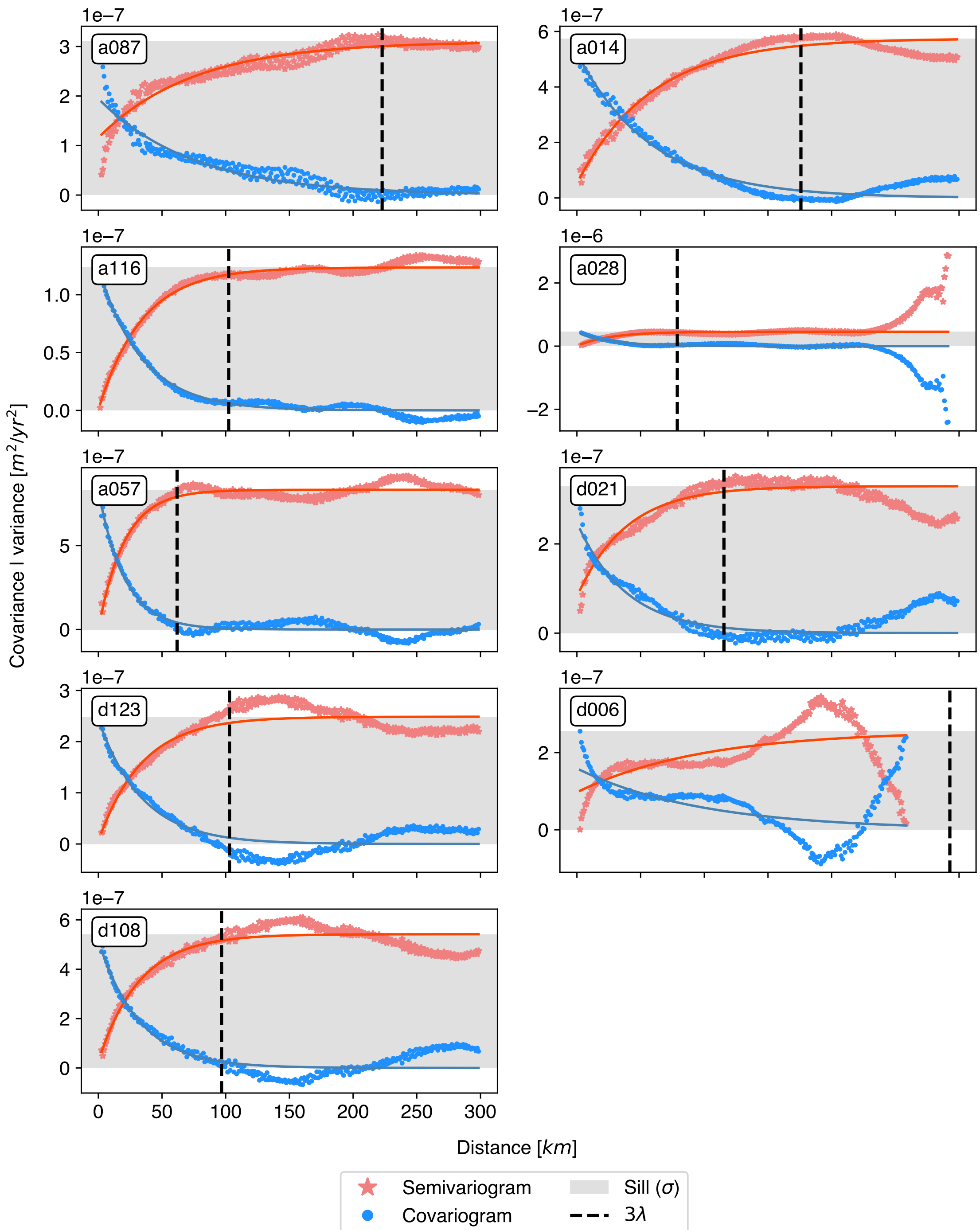

Figure S6. Sample semi-variograms and covariograms. The exponential functions fitted the sample covariograms. The sill σ is marked by the grey band. The value of σ is used to fill in the diagonals of the covariance matrix, $\mathbf{C}_{\mathrm{d_s}}$. Three times of the characteristic length scales λ is marked by the dashed line. See Suppl. Text S4-2.

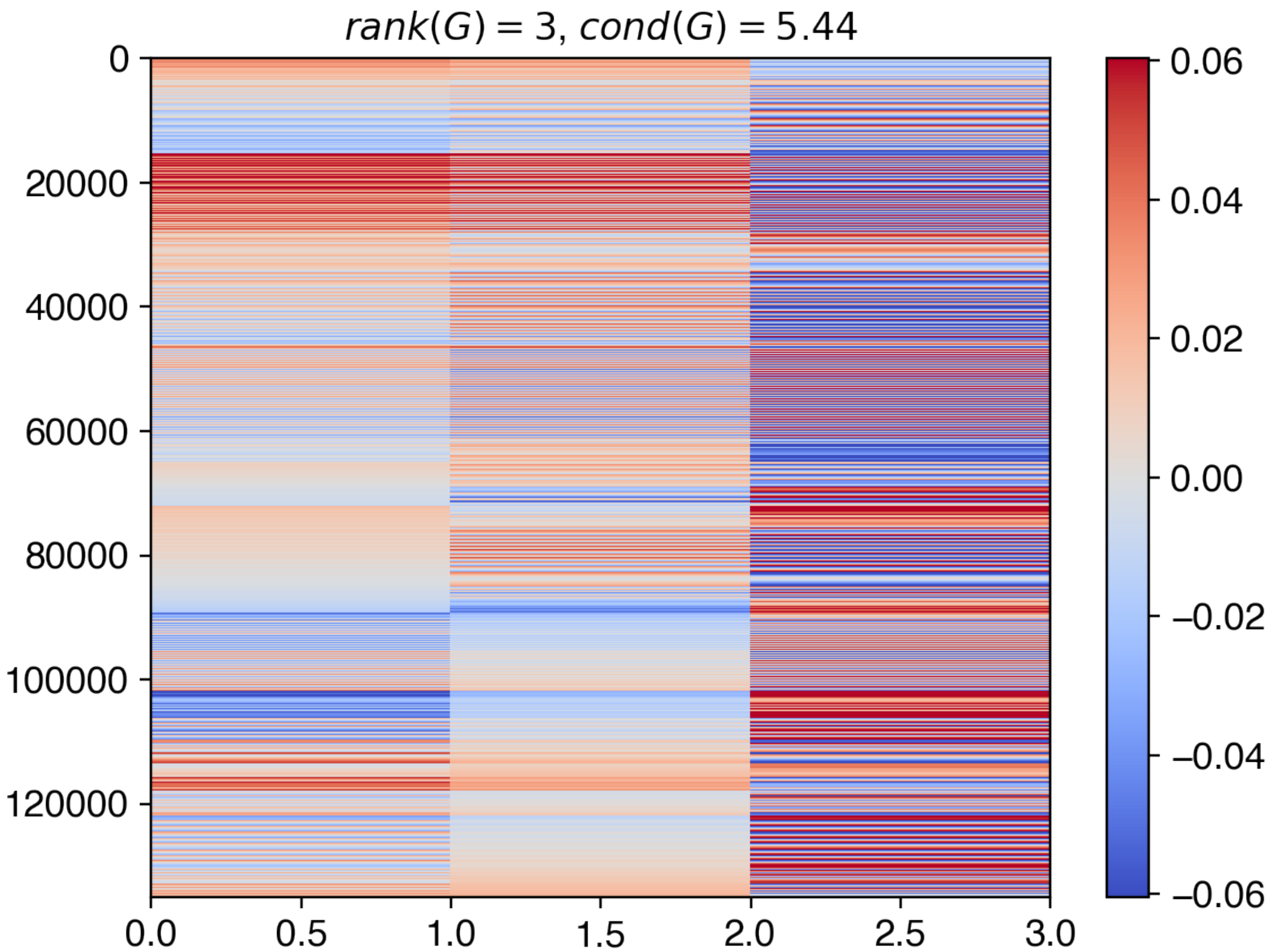

Figure S7. The linear operator **G**, which transforms the Cartesian rotation parameters to the nine InSAR LOS velocities, normalized by the Earth's radius 6378.137 km. See Suppl. Text S3-1.

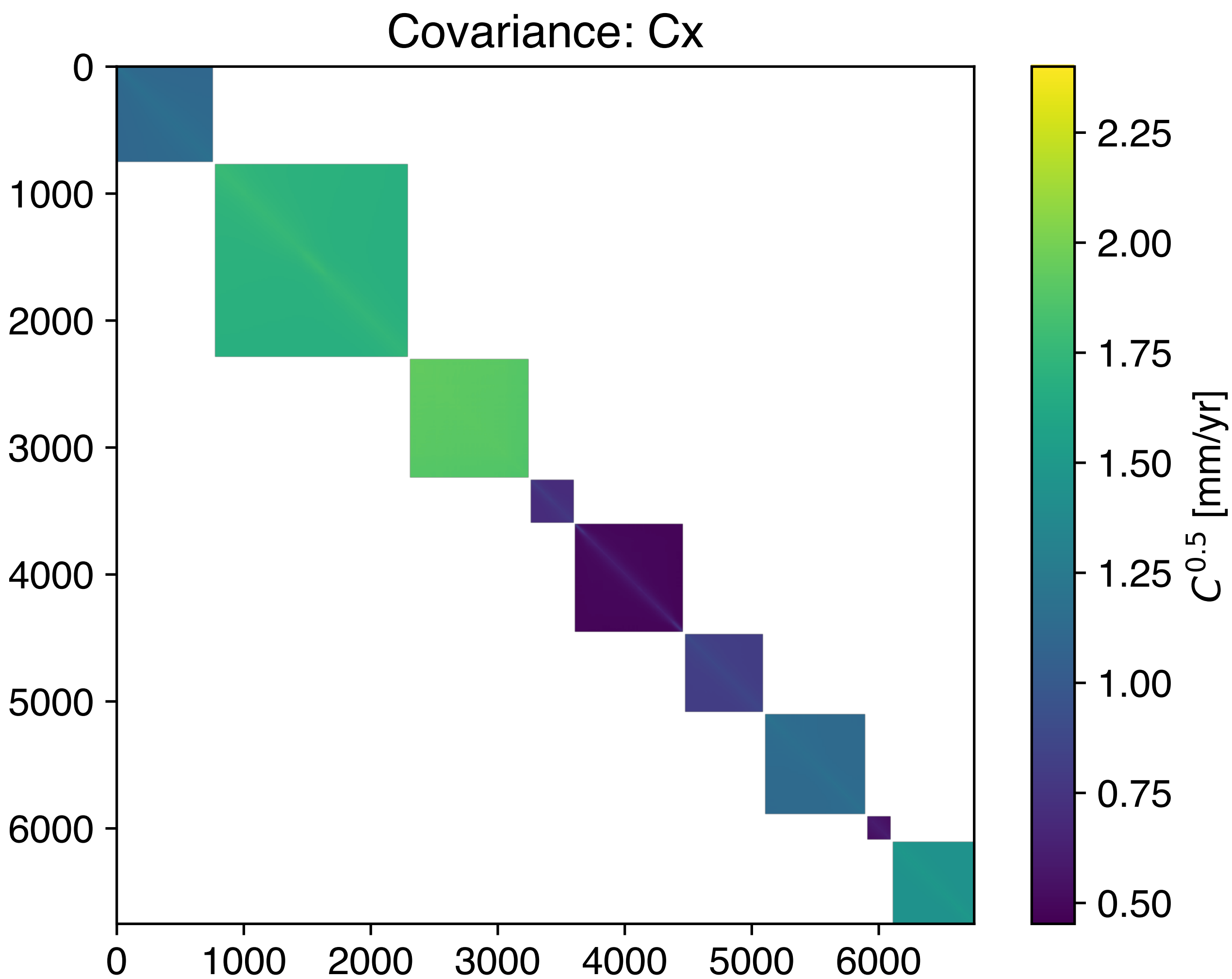

Figure S8. The data covariance matrices $\mathbf{C}_\chi = \mathbf{C}_\mathrm{d} + \mathbf{C}_\mathrm{p}$. To display the variability of dynamic range, the color bar shows the squared root of $\mathbf{C}_\chi$. The observational covariance is composed of the temporal term, $\mathbf{C}_{\mathrm{d}_\mathrm{t}}$ based on the prior-selected reference points (Figure S2), and the spatial term, $\mathbf{C}_{\mathrm{d}_\mathrm{s}}$ from the semi-variograms (Figure S6). $\mathbf{C}_\mathrm{p}$ quantifies the uncertainty due to the reference point, see Main Text Section 2.3 and Suppl. Text S3-2.

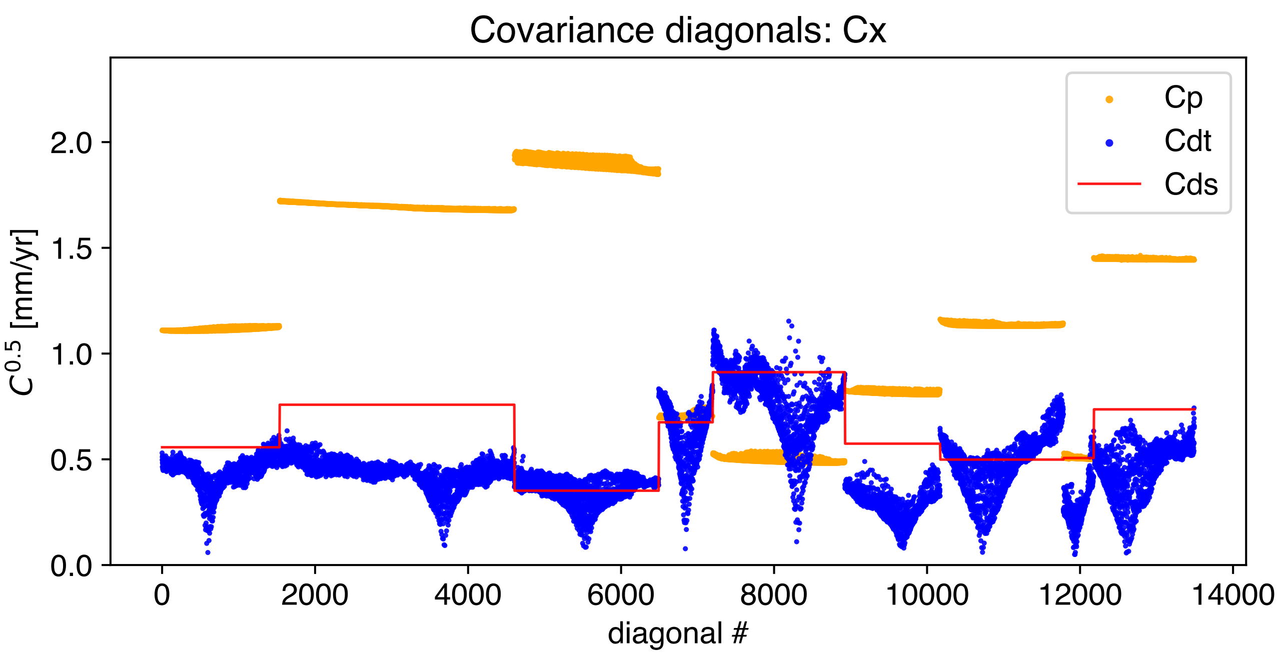

Figure S9. The diagonals of the covariance matrices in Figure S8. The values displayed here are the squared roots of the covariance for plotting purposes. The blue dots indicate the diagonals of $\mathbf{C}_{\mathrm{d_t}}$, in which the lowest point marks the chosen reference pixel in each track in this realization. The red line indicates the diagonals of $\mathbf{C}_{\mathrm{d_s}}$, which is constant within each velocity track. The orange dots indicate the epistemic uncertainty, $\mathbf{C}_{\mathrm{p}}$, of the reference point estimated from the entire 1,000 realizations.

Figure S10. Caption next page.

Figure S10. Euler fitting results. Rows from top to bottom: Observed velocity, velocity standard deviation, the velocity field from the estimated Euler pole, post-fit residual velocity, the velocity predicted from the ITRF2014 plate motion model, the difference between our pole and the ITRF2014 pole. See the Main Text Figure 3 and the pole marked by “x” in Figure 4.

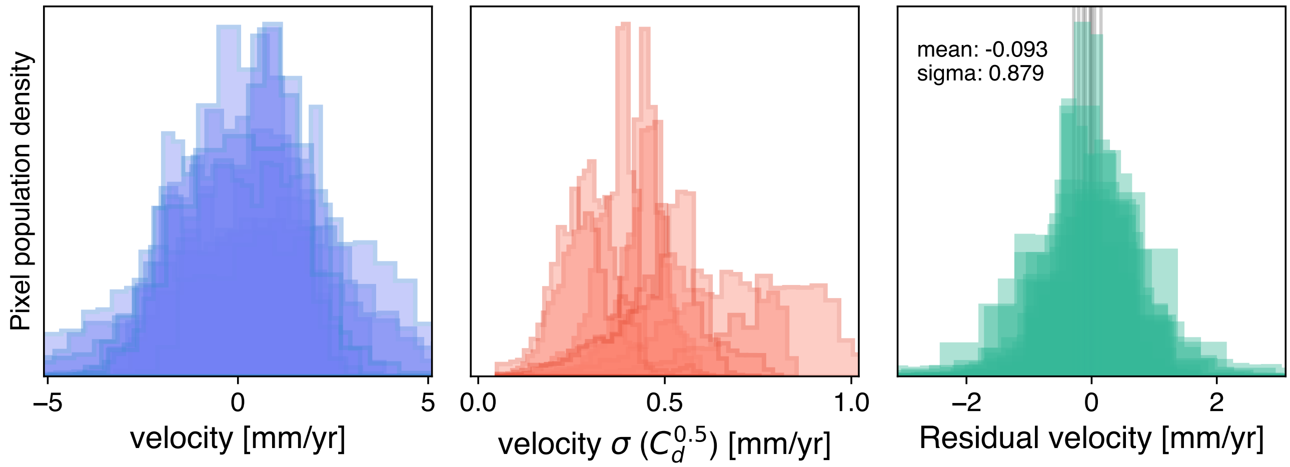

Figure S11. The histograms of velocities, standard deviations, and post-fit residuals, for all the tracks. These corresponds to the data and post-fit residuals in Figure S10.

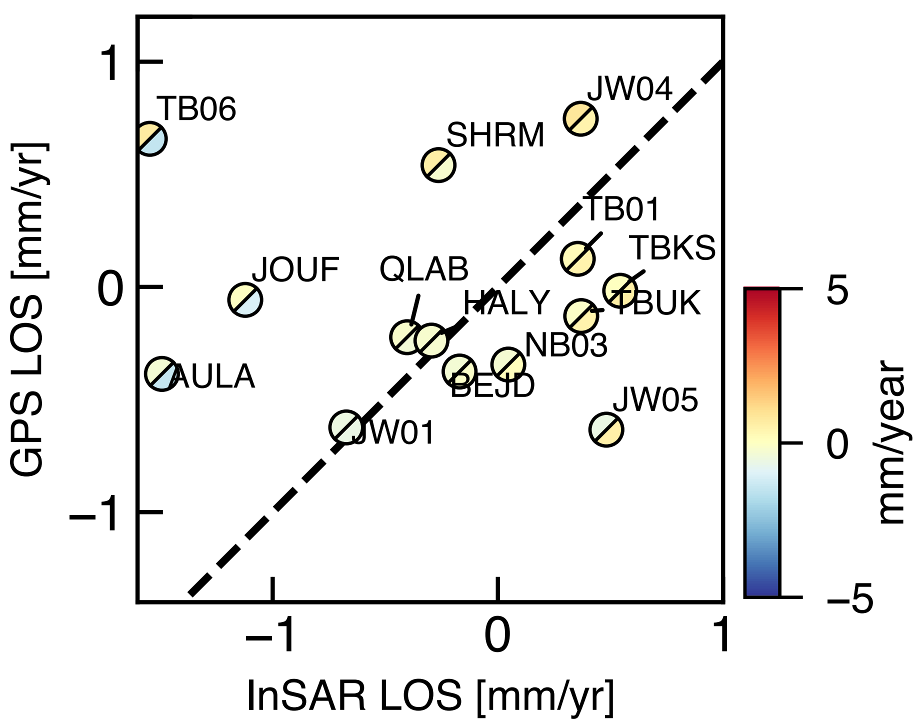

Figure S12. The comparison with GPS horizontal velocities projected to LOS in the Arabian-fixed reference frame. Values are taken from the Main Text Figure 3d.

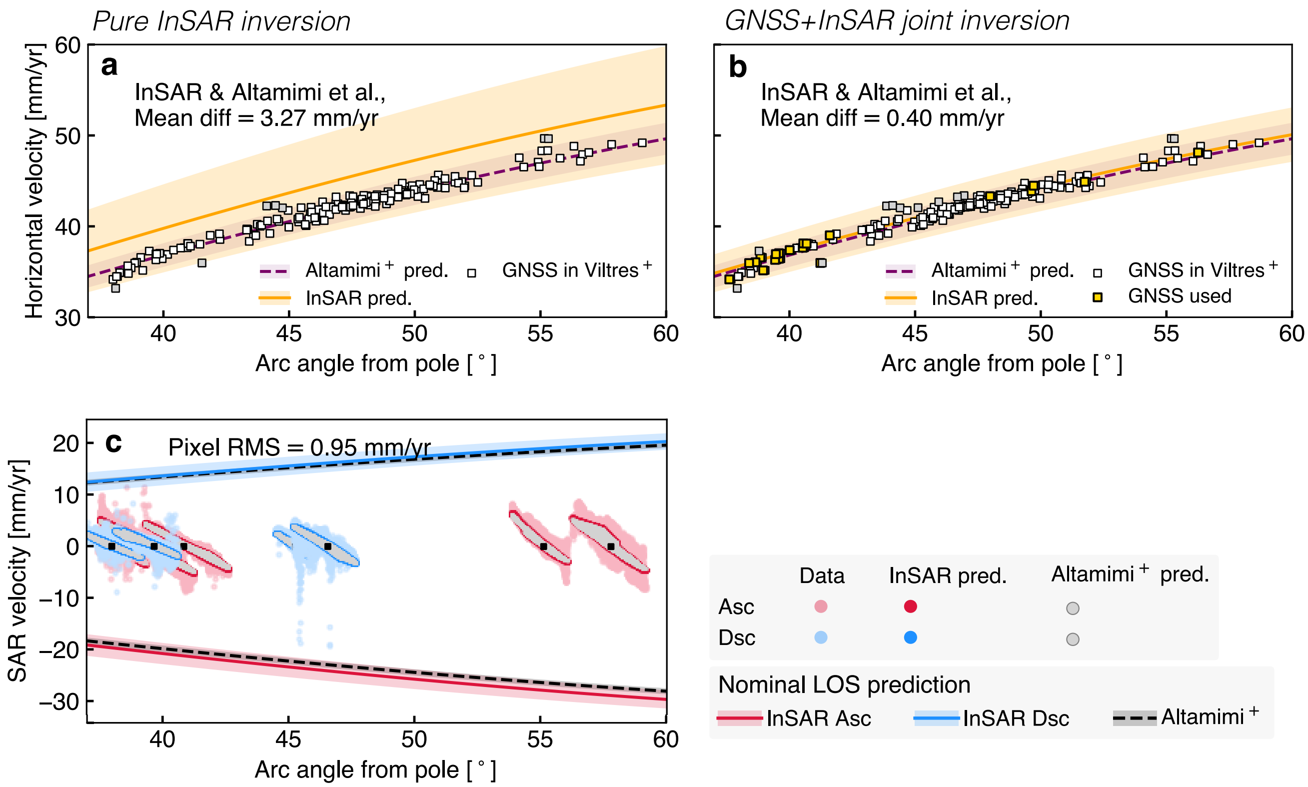

Figure S13. Profiles horizontal velocities tangential to the plate motion direction of the ITRF2014 Arabia model (Altamimi et al., 2017). The x-axis is the great-arc angle from the ITRF2014 pole. **(a)** The pure InSAR-derived pole is the posterior after considering the ensemble of the random reference points in the Main Text. **(b)** The joint inversion with InSAR-collocated GNSS stations taken from the network (white squares) in Viltres et al. (2022). The outlier sites (outside the 2-sigma bound of Altamimi et al., prediction; the grey squares) are stations close to the Afar rifting zone and the Dead Sea Transform. **(c)** The line-of-sight (LOS) velocities from nine InSAR tracks. The red and blue scatter dots are ascending and descending pixel-wise LOS velocities in each track, with lighter color indicating the observations and darker color the posterior pole predictions. The grey dots is the prediction from Altamimi's pole using the same pixel-wise LOS geometries. The lines indicate the predicted LOS velocity profiles using a nominal LOS geometry across the plate. Red and blue lines are InSAR's posterior predictions, while the grey line is predicted using Altamimi's pole.

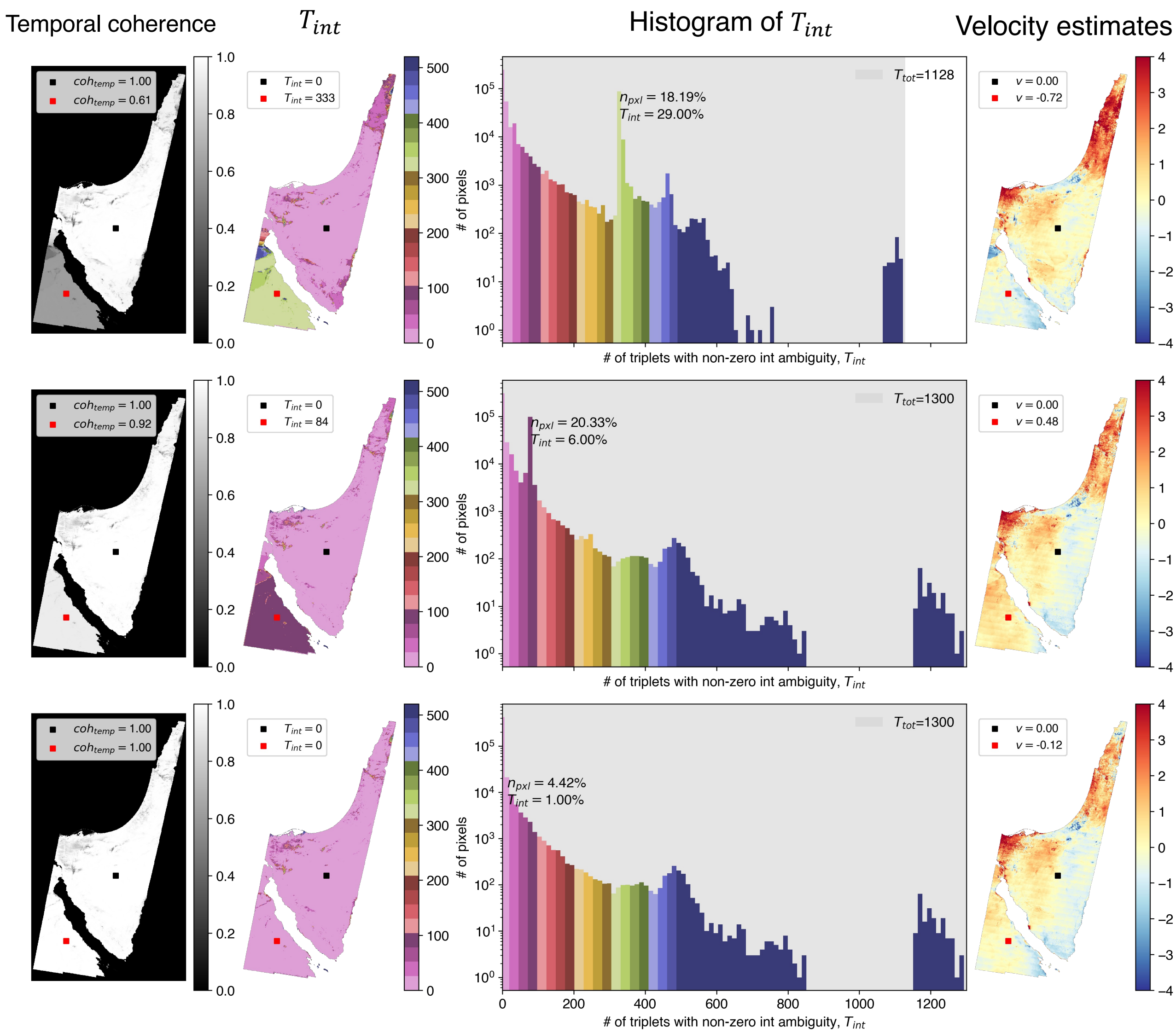

Figure S14. The correction of unwrapping errors using phase misclosure, demonstrated using descending track D094 in the Sinai Peninsula. Top: the original interferometric stack following the processing workflow described in Main Text Section 2.1. Middle: The results from a stack of interferograms with tropospheric model subtracted before unwrapping. Bottom: The results from a stack of interferograms with both model and ionospheric delays subtracted before unwrapping, then apply the phase-closure unwrapping error correction based on T_{int}, as described in Supplementary Text S3. We can visually see unwrapping errors in the temporal coherence and the velocity fields. The data from this orbital track is not used in the Main Text.